2 Fundamentals

A brief description of the SEVIRI instrument aboard MSG will be given at the beginning of this chapter. Differences between cloudy and clear sky conditions will be described in respect to their spectral and temporal signatures in the SEVIRI channels the developed cloud detection algorithm is based on. The investigations of spectral cloud and clear sky characteristics will point at several potential tests usable for cloud detection. These tests will not be specified any further by deriving thresholds or the likes because, as described in chapter 4, the developed cloud detection algorithm analyzes the spectral information exclusively by means of artificial neural networks (NN). In this chapter, neural network input parameters with physical relevance will be identified.

The analysis of time series under clear sky conditions in the last part of this chapter is the basis for the "assumed clear sky brightness temperature estimation" (ACSBTE) algorithm (chapter 3) which is a central input parameter for the developed neural networks.

This chapter is also helpful for identifying weaknesses and strengths of the developed methods.

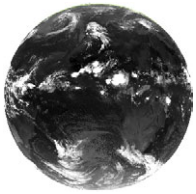

2. 1 SEVIRI aboard MSG

In August 2002, MSG was successfully launched by Arianespace as a successor of METEOSAT-7 and was placed into a geostationary orbit, 36000 *km* above the equator. The dissemination trial of HRIT[1] formatted level 1.5 data via EUMETSAT's broadcast system for environmental data EUMETCast [*EUMETSAT*, 2004b] started in May 2003. After spacecraft decontamination and spacecraft shift from -10.5° *E* to its final position -3.4° *E* the dissemination trial was completed and routine operation of MSG started at the end of January 2004. To ensure constant 0.0° *E* viewing geometry, every picturing level 1.0 raw data broadcasted by MSG is geometrically rectified and radiometrically calibrated before being disseminated to end users via the Hotbird 6 satellite of the Deutsche Telekom.

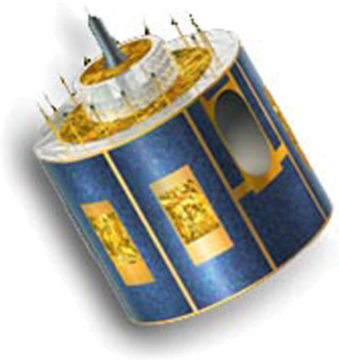

Figure 2-1: The MSG satellite (image from *www.eumetsat.int*).

MSG encloses the scientific instruments GERB (**g**eostationary **e**arth **r**adiation **b**udget), a visible and infrared radiometer for earth radiation studies [*Harries and Crommelynck,* 1999] and the "**s**pinning **e**nhanced **v**isible and **i**nfra**r**ed **i**mager" SEVIRI. The latter represents the satellite's main payload.

As illustrated in figure 2-2 SEVIRI covers the visible (*HRV*, VIS_{006}, VIS_{008}), the near infrared (NIR_{016}), and the thermal infrared spectral region (IR_{039}, IR_{062}, IR_{073}, IR_{087}, IR_{097}, IR_{108}, IR_{120}, IR_{134}) with twelve channels. The channels' radiometric accuracy is

1) HRIT (**h**igh **r**ate **i**nformation **t**ransmission) is a file format based on 10 bit wavelet and 12 bit JPEG (**j**oint **p**hotographic **e**xperts **g**roup) compression. A detailed format description can be found in *EUMETSAT* [2005].

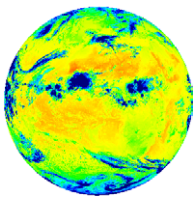

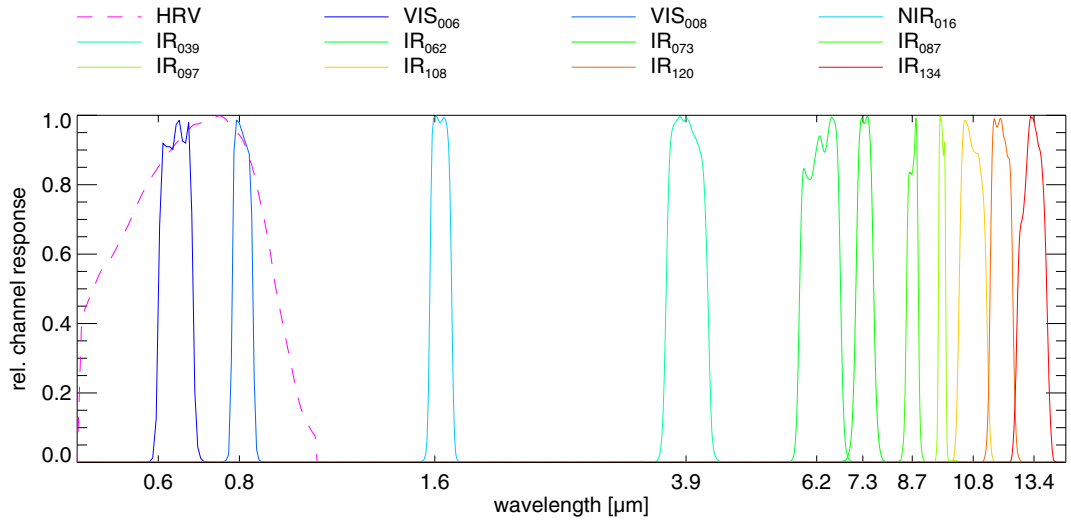

Figure 2-2: Spectral response functions of the SEVIRI channels [*EUMETSAT*, 2004d].

channel	noise budget
HRV	$0.63\,W\,m^{-2}\,sr^{-1}\,\mu m^{-1}$
VIS_{006}	$0.27\,W\,m^{-2}\,sr^{-1}\,\mu m^{-1}$
VIS_{008}	$0.21\,W\,m^{-2}\,sr^{-1}\,\mu m^{-1}$
NIR_{016}	$0.07\,W\,m^{-2}\,sr^{-1}\,\mu m^{-1}$
IR_{039}	$0.17K$ at $300\,K$
IR_{062}	$0.21K$ at $250K$
IR_{073}	$0.12K$ at $250K$
IR_{087}	$0.10K$ at $300\,K$
IR_{097}	$0.29K$ at $255K$
IR_{108}	$0.11K$ at $300\,K$
IR_{120}	$0.15K$ at $300\,K$
IR_{134}	$0.37K$ at $270K$

Table: 2-1: Noise-equivalent radiances and temperatures for the solar channels and thermal infrared channels, respectively, of the SEVIRI instrument on MSG at referenced target temperature [*Schmetz et al.*, 2002b].

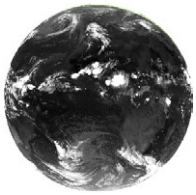

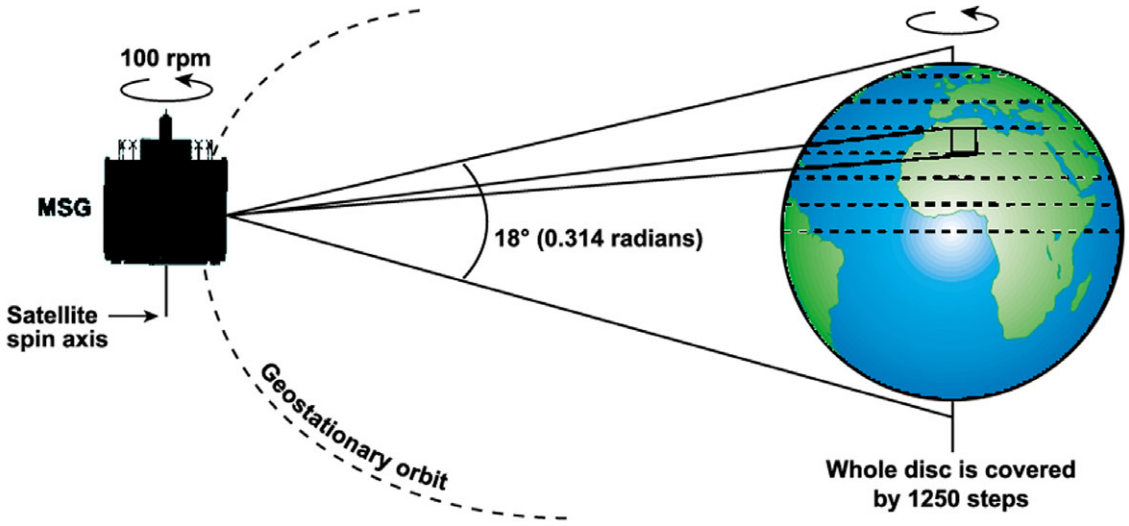

Figure 2-3: Imaging technique of SEVIRI aboard MSG [*EUMETSAT,* 2001]. The satellite rotation of 100 *rpm* combined with stepwise tilting a scan mirror performs line by line scanning of the earth.

given in table 2-1. An overview of possible data interpretation of those channels with regard to several different remote sensing applications is given in *EUMETSAT* [2004e] and briefly in *Schmetz et al.* [2002a].

According to *Schmetz et al.* [2002a], the high resolution visible channel offers a spatial resolution of 1.67 *km* and a sampling distance of 1 *km* at sub satellite point. The corresponding values for the other three solar and the eight thermal infrared channels are a 4.8 *km* spatial resolution and 3 *km* sampling distance. The absolute accuracy of the pixel locations is better than 3 *km* and the image to image relative accuracy is 1.2 *km*. The inter channel registration is specified by 0.75 *km* for the thermal infrared channels and 0.6 *km* for the solar channels.

Analog to earlier METEOSAT satellites, the imaging of MSG is performed by scanning the earth line by line via combining the satellite spin of 100 *rpm* with stepwise tilting a scan mirror (figure 2-3). The resulting images measure 11 136 times 5 568 pixels for the *HRV* channel and 3 712 times 3 712 pixels for the remaining channels. As the low

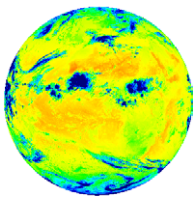

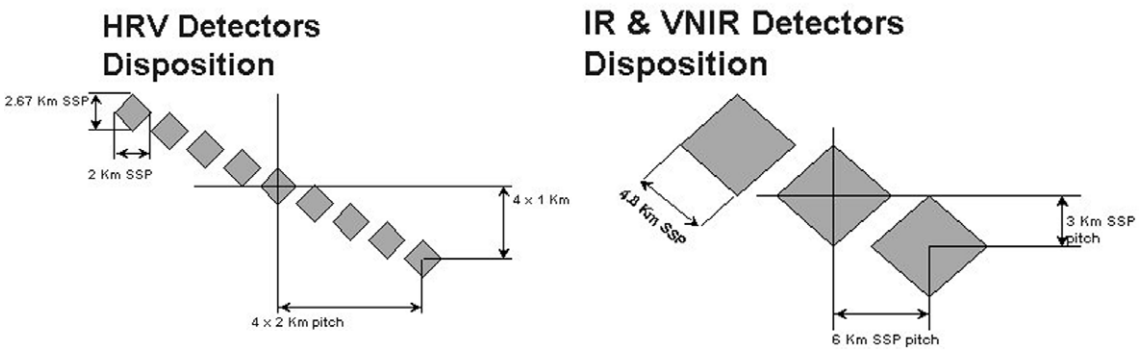

Figure 2-4: Each SEVIRI channel consists of three respectively nine detectors. Their disposition is illustrated in this figure [*EUMETSAT,* 2001].

resolution SEVIRI channels consist of three and the high resolution channel consist of nine detectors (figure 2-4), it is possible to scan the whole disk in approximately twelve minutes. The routine dissemination interval amounts to 15 minutes.

In the framework of this dissertation, a receiving station has been set up according to *EUMETSAT* [2004b]. A near real time product processing software environment has been established based on the programming language IDL.

With a digitalization depth of 10 bit, 12 bit for the *HRV* channel respectively, SEVIRI produces an amount of about 25 GB raw data per day. Due to compression, this results in about 7 GB of level 1.5 data disseminated to the end users. Since the beginning of the dissemination trial phase in May 2003, this data stream is operationally received by the *Institut für Weltraumwissenschaften*, then converted to more user friendly formats[1], stored, and processed to higher products.

The flip-book animation at the bottom of the right pages (odd page numbers) illustrates how SEVIRI "sees" the earth. When taking a closer look at the animation, not only the movement of the day/night border but also of some cloud systems and sun glint is visible.

1) The converted level 1.5 data is stored in PNG (**p**ortable **n**etwork **g**raphics) and JPEG files. Corresponding additional information (e. g. calibration coefficients) is stored in XML (e**x**tensible **m**arkup **l**anguage) formatted files.

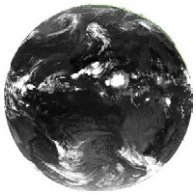

The images are quasi true color composites of the channels VIS_{006}, VIS_{008}, VIS_{016} (color rotated and weighted by IR_{108}) from June, 07th 2004, 00:00 to 23:45 UTC. The flip-book animation at the bottom of the left pages (even page numbers) is described in chapter 3.

2. 2 The radiative transfer equation

The amount of incoming radiation at the satellite's detectors can be calculated by solving the radiative transfer equation. Referring to *Jacobson* [1999], for a homogenous atmospheric layer with infinitesimal depth $\mathrm{d}S_b$ the radiative transfer equation is specified by the change of spectral radiance $\frac{\mathrm{d}L_{\lambda,\mu,\phi}}{\mathrm{d}S_b}$:

$$\frac{\mathrm{d}L_{\lambda,\mu,\phi}}{\mathrm{d}S_b} = -\frac{\mathrm{d}L_{so,\lambda}}{\mathrm{d}S_b} - \frac{\mathrm{d}L_{ao,\lambda}}{\mathrm{d}S_b} + \frac{\mathrm{d}L_{si,\lambda,\mu,\phi}}{\mathrm{d}S_b} + \frac{\mathrm{d}L_{Si,\lambda,\mu,\phi}}{\mathrm{d}S_b} + \frac{\mathrm{d}L_{ei,\lambda}}{\mathrm{d}S_b} \qquad (2\text{-}1)$$

where λ denotes a specific wavelength and μ, ϕ the beam direction (cosine of beam zenith angle, beam azimuth angle). The summands of (2-1) are explained in the following:
Scattering of radiation out of the beam:

$$\frac{\mathrm{d}L_{so,\lambda}}{\mathrm{d}S_b} = \sigma_{s,\lambda} L_{\lambda,\mu,\phi} \qquad (2\text{-}2)$$

Absorption of radiation along the beam:

$$\frac{\mathrm{d}L_{ao,\lambda}}{\mathrm{d}S_b} = \sigma_{a,\lambda} L_{\lambda,\mu,\phi} \qquad (2\text{-}3)$$

Multiple scattering of diffuse radiation into the beam:

$$\frac{\mathrm{d}L_{si,\lambda,\mu,\phi}}{\mathrm{d}S_b} = \sum_k \left(\frac{\sigma_{s,k,\lambda}}{4\pi} \int_0^{2\pi} \int_{-1}^{1} L_{\lambda,\mu',\phi'} P_{s,k,\lambda,\mu,\mu',\phi,\phi'} \, \mathrm{d}\mu' \, \mathrm{d}\phi' \right) \qquad (2\text{-}4)$$

Single scattering of direct solar radiation into the beam:

$$\frac{\mathrm{d}L_{Si,\lambda,\mu,\phi}}{\mathrm{d}S_b} = F_{s,\lambda} e^{-\tau_\lambda / \mu_s} \sum_k \left(\frac{\sigma_{s,k,\lambda}}{4\pi} P_{s,k,\lambda,\mu,-\mu_s,\phi,\phi_s} \right) \qquad (2\text{-}5)$$

Emission of infrared radiation into the beam:

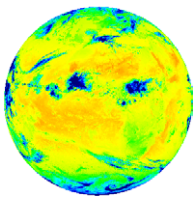

$$\frac{\mathrm{d}L_{ei,\lambda}}{\mathrm{d}S_b} = \sigma_{a,\lambda} B_{\lambda,T} \tag{2-6}$$

The meaning of the parameters in (2-2) - (2-6) are: $\sigma_{s,\lambda} = \sigma_{s,g,\lambda} + \sigma_{s,a,\lambda} + \sigma_{s,c,\lambda}$ equals the sum of the **s**cattering coefficients for **g**as (Rayleigh), **a**erosol and **c**loud droplets. The definition for the **a**bsorption coefficient $\sigma_{a,\lambda}$ is analog. In (2-4) and (2-5) k indexes gas, aerosol and cloud. In the following chapters indices for gas, aerosol and cloud droplets are omitted and if not explicitly mentioned, cloud droplets are implied. P_s represents the scattering phase function, that gives the angular distribution of scattered energy as a function of the incident and scattered beam direction. Integration over $\mathrm{d}\mu'\mathrm{d}\phi'$ means integration over the solid angle. F_s gives the incident solar radiation and $-\mu_s$ and ϕ_s its direction. τ stands for the optical thickness and B for the radiation emitted by a black body with the temperature T. B is given by Planck's law:

$$B_{\lambda,T} = \frac{2\,h\,c^2}{\lambda^5}\left(e^{\frac{h\,c}{\lambda\,k_B\,T}} - 1\right)^{-1} \tag{2-7}$$

including the vacuum light speed c, Boltzmann's constant k_B and Planck's constant h.

Top of atmosphere radiances can be derived by solving equation (2-1) by integrating over the height of the atmosphere under presumption of suitable boundary conditions at the surface. The radiative transfer simulation programs MOMO (**m**atrix-**o**perator-**mo**dell) (first introduced in *Fischer and Grassl* [1984]) and XTRA (e**x**tended line-by-line atmospheric **t**ransmittance and **r**adiance **a**lgorithm) (first introduced in *Rathke and Fischer* [2000]), both developed and in common use at the *Institut für Weltraumwissenschaften*, are solving this integral equation under different assumptions. As MOMO has been developed for simulating radiative transfer in the solar spectral region, it neglects thermal emission processes. XTRA neglects molecular scattering and solar radiation as it has been designed for the thermal infrared spectral region.

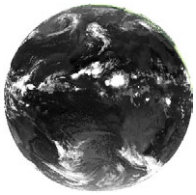

2. 3 Converting radiances to brightness temperatures

As given by *Schmetz et al.* [2002c], the conversion from the radiance L_{ch} measured by a thermal infrared channel IR_{ch} to an equivalent brightness temperature BT_{ch} is performed through an analytic relationship related to the inversion of Planck's law (2-7):

$$BT_{ch} = \left[\frac{h\ c\ \nu_{c,\,ch}}{k_B\ log(1 + 2\ h\ c^2\ \nu_{c,\,ch}^3 / L_{ch})} - b_{ch} \right] / \ a_{ch} \qquad (2\text{-}8)$$

In this equation $\nu_{c,\,ch}$ represents the channel's central wavenumber, while a_{ch} and b_{ch} are the so-called band correction coefficients provided by EUMETSAT which account for the channel's spectral response function (figure 2-2). Conversion to brightness temperatures simplifies the data interpretation because the brightness temperature spectrum of a black body is given by one constant temperature value. In this way, spectral effects of surface, atmosphere or clouds are interpretable as deviation from a constant.

2. 3. 1 Sensitivity to the target emissivity

The emissivity ε_λ affects the amount of radiation emitted by the observed target by:

$$L_{target,\,\lambda} = \varepsilon_\lambda\ B_{\lambda,\,T} \qquad (2\text{-}9)$$

Therefore, the emitted radiance is a function of the target temperature and also of the target emissivity. The measured brightness temperature equals the target temperature only when observing a black body (neglecting atmospheric effects). As given in (2-9), the channel's measured radiance is linear to the target emissivity. Due to the non-linearity of the inverse of Planck's function and therefore also of (2-8), the brightness temperatures measured at different central wavelengths differ in their sensitivity to the target

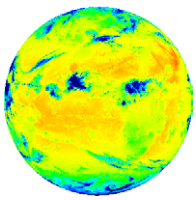

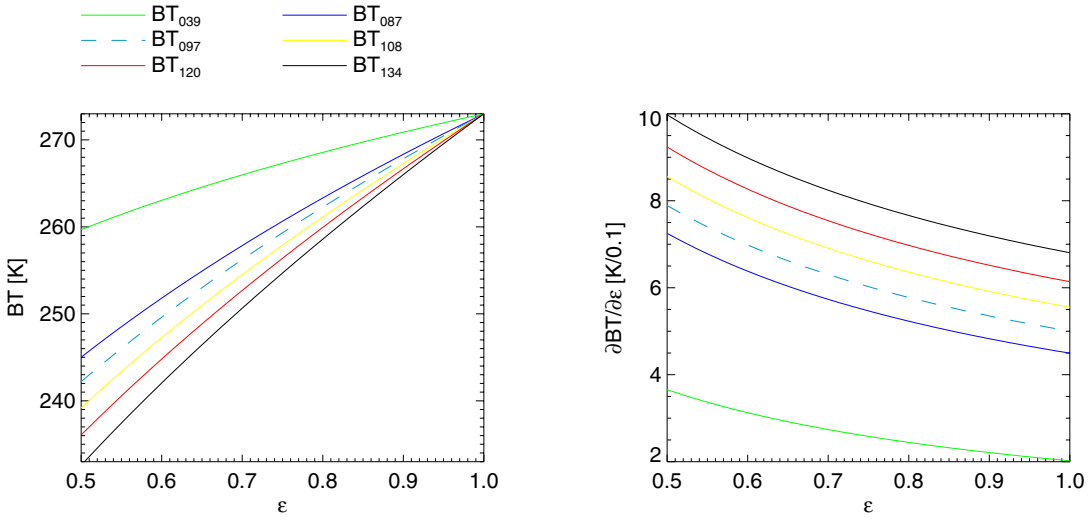

Figure 2-5: The **left** figure shows the relation between target emissivity and measured brightness temperature of several SEVIRI channels. The sensitivity to the emissivity is given by the **right** figure. Both figures have been created simply by applying Planck's function and its inverse (no atmospheric effects). The figures show that the brightness temperatures of channels at longer wavelengths are much more sensitive to target emissivity changes.

emissivity. Figure 2-5 illustrates the relation of target emissivity and channel brightness temperature. It shows that the brightness temperatures measured by channels at longer wavelengths are much more sensitive to target emissivity changes.

2. 3. 2 Sensitivity to sub pixel temperature fraction

Due to the non-linearity of Planck's function (2-7), the channel brightness temperatures are not linear to the sub pixel temperature fraction and also differ in their sensitivity to this parameter. Figure 2-6 illustrates the relation of the measured channel brightness temperatures and the sub pixel temperature fraction when observing a pixel consisting of one part at $250K$ and the other part at $300K$. Particularly BT_{039} seems to be very sensitive to hot spots (low fraction) and insensitive to cold spots (high fraction) in its field of view so that the warmer parts are dominating the measured brightness temperature signal.

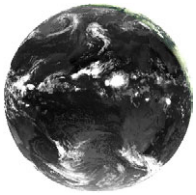

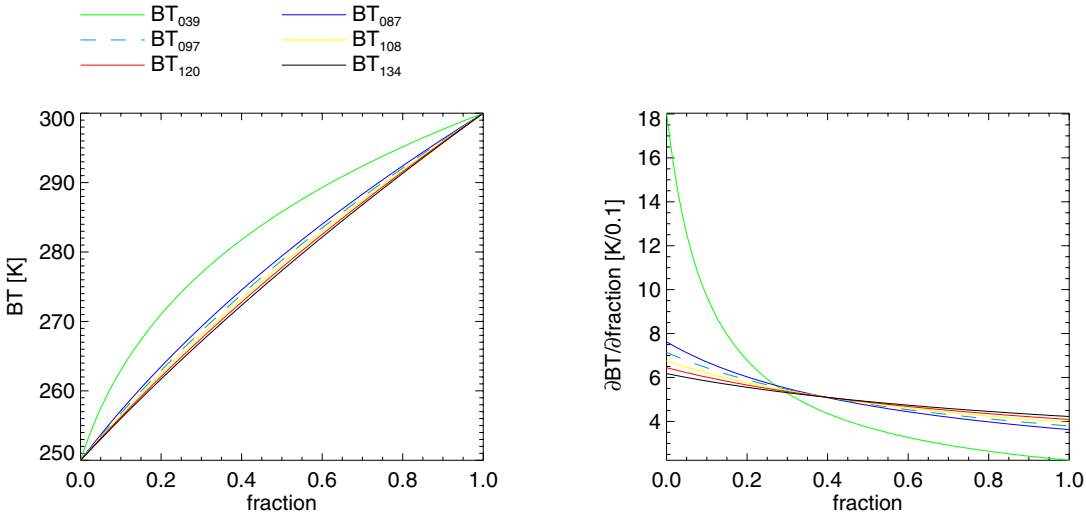

Figure 2-6: The **left** figure shows the channel brightness temperatures depending on the sub pixel temperature composition when observing a pixel consisting of one part at $250\,K$ and the other part at $300\,K$ The sensitivity to the fraction is given by the **right** figure. As in figure 2-5, these figures have been created simply by applying Planck's function and its inverse (no atmospheric effects).

2. 4 Spectral features of clouds, atmosphere, and surfaces in the SEVIRI channels

2. 4. 1 Emission and reflection of surfaces

The radiance emitted by surfaces can be calculated from (2-9). For opaque media, the relation of absorption a_λ and reflection r_λ coefficients are given by:

$$1 = a_\lambda + r_\lambda \tag{2-10}$$

Kirchoff's law applies for thermodynamic equilibrium:

$$a_\lambda = \varepsilon_\lambda \tag{2-11}$$

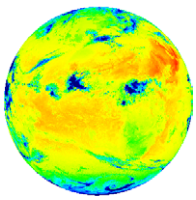

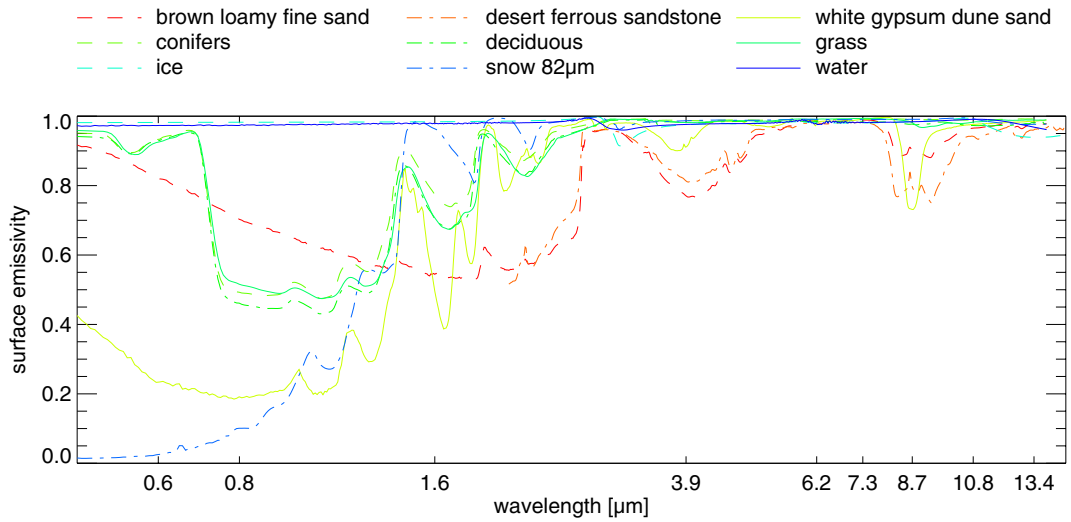

Figure 2-7: Emissivity of some common surface types calculated according to (2-12) from reflectivity spectra of the ASTER spectral library [e.g. *Salisbury and D'Aria*, 1992, 1994; *Salisbury et al.*, 1994].

Consequently, the reflection index follows from (2-10) and (2-11):

$$r_\lambda = 1 - \varepsilon_\lambda \qquad (2\text{-}12)$$

Exemplarily, figure 2-7 gives some emissivity spectra of several common surface types. The corresponding reflectivity spectra can be calculated from (2-12). Additional information on surface emissivities as well as on their classification from satellites are given e.g. in *Snyder et al.* [1998].

2. 4. 2 Optical properties of air

The efficiency of radiation extinction by Rayleigh scattering is proportional to λ^{-4}. The optical thickness of an aerosol and cloud free atmosphere can be estimated with 0.07 at 0.6 µm, 0.02 at 0.8 µm, and only 0.001 at 1.6 µm. As clouds and also aerosols generally

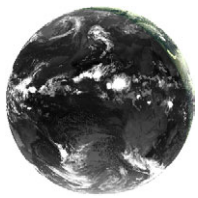

cause substantially higher values of optical thickness at these wavelengths, molecular scattering is neglected in this phenomenological description of the optical properties of air.

Assuming a simplified atmosphere which only interacts with radiation by absorption and emission processes, neglecting scattering by molecules, cloud droplets, and aerosols, the radiative transfer equation (2-1) is reduced to the terms (2-3) and (2-6). For radiative transfer simulations, XTRA computes the total transmittance by means of absorption coefficients taken from HITRAN (**hi**gh-resolution **tran**smission molecular absorption database) [*Rothman et al.,* 2003]. In order to illustrate how the SEVIRI channels are affected by molecular absorption, the total transmissivity of a non-scattering US standard atmosphere [*McClatchey et al.*, 1972] and of its most absorbing constituents (water vapor, carbon dioxide, and ozone) has been calculated (figure 2-8). The sensitivity of the measured brightness temperatures BT_{039}, BT_{087}, BT_{097}, BT_{108}, BT_{120}, and BT_{134} to these constituents has also been derived by XTRA simulations for a US standard atmosphere. The results are given in figure 2-9. With a sensitivity of up to $-2.5\,K/(g/cm^2)$ the channel brightness temperatures BT_{087}, BT_{108}, BT_{120}, and BT_{134} are most sensitive to water vapor. BT_{097} shows a very high sensitivity to ozone with up to $-0.9\,K/10\,DU$ (DU=Dobson unit). The sensitivity to carbon dioxide is by far highest for BT_{134} with up to $-0.21\,K/10ppm$. In general, atmospheric water vapor varies world wide between about 0 and 5 g/cm^2. Typical O_3 amounts in SEVIRI's field of view are in the range of 160 and 480DU. The inter annual variability of CO_2 is approximately 7ppm.

2. 4. 3 Optical properties of clouds

The description of spectral cloud features in this subsection is limited to non-raining clouds whose droplet effective radii are less than approximately 20μm [*Gerber,* 1996]. Furthermore, spherical particles are assumed so that their optical properties in the spectral range of the SEVIRI channels can be calculated from Mie's solution to Maxwell's

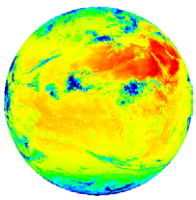

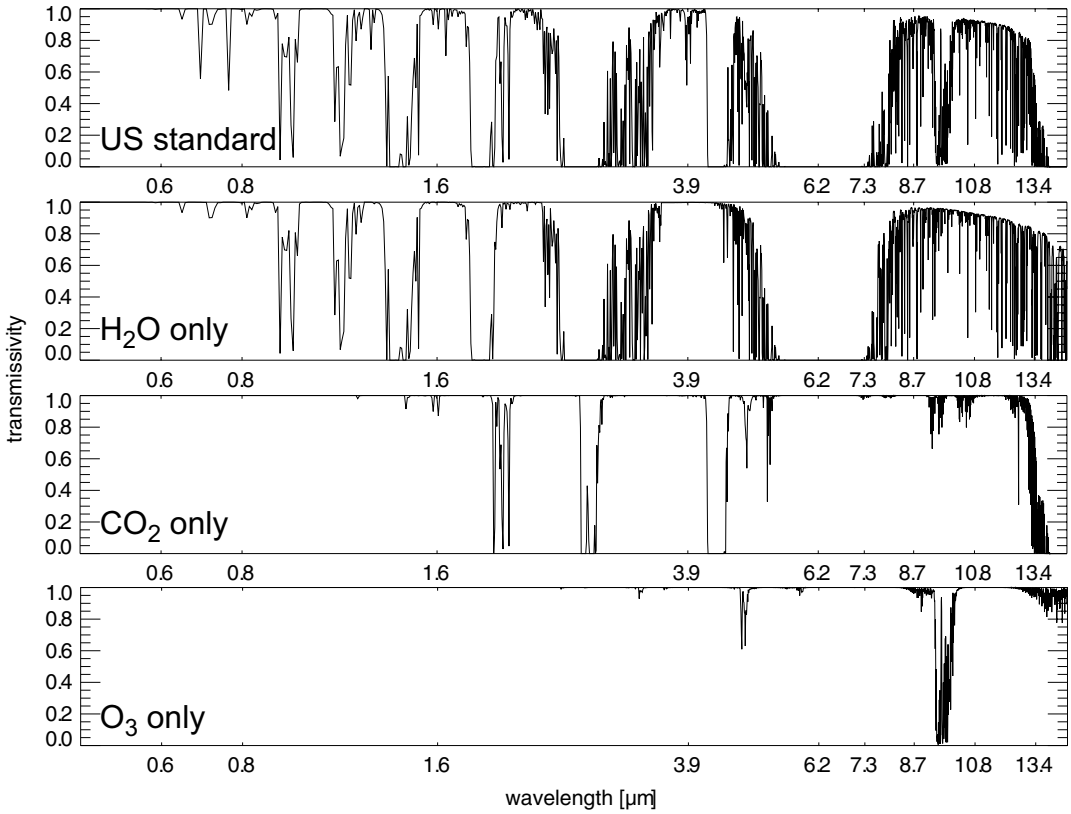

Figure 2-8: Total transmissivity of the earth atmosphere and some of its most absorbing constituents derived by XTRA calculations for a US standard atmosphere neglecting Rayleigh scattering.

equations for spheres [*Mie*, 1908]. The algorithm used for the Mie-calculations is based on *Wiscombe* [1980]. According to *Hansen* [1971], a modified gamma particle size distribution function has been chosen for all Mie calculations of any utilized XTRA simulation of cloudy atmospheres.

In addition to the size distribution, the complex refraction index of the scattering medium is the most important input parameter to Mie calculations. The refraction index dataset for liquid water given by *Downing and Williams* [1975] has been chosen according to *Rathke* [2000]. As this dataset was only available for droplet radii from 2 to 15 μm it has been extended by the dataset given by *Segelstein* [1981]. For ice, the dataset given by *Warren* [1984] has been used. Both, the imaginary part, primary affecting absorption, and

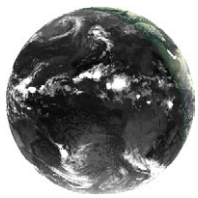

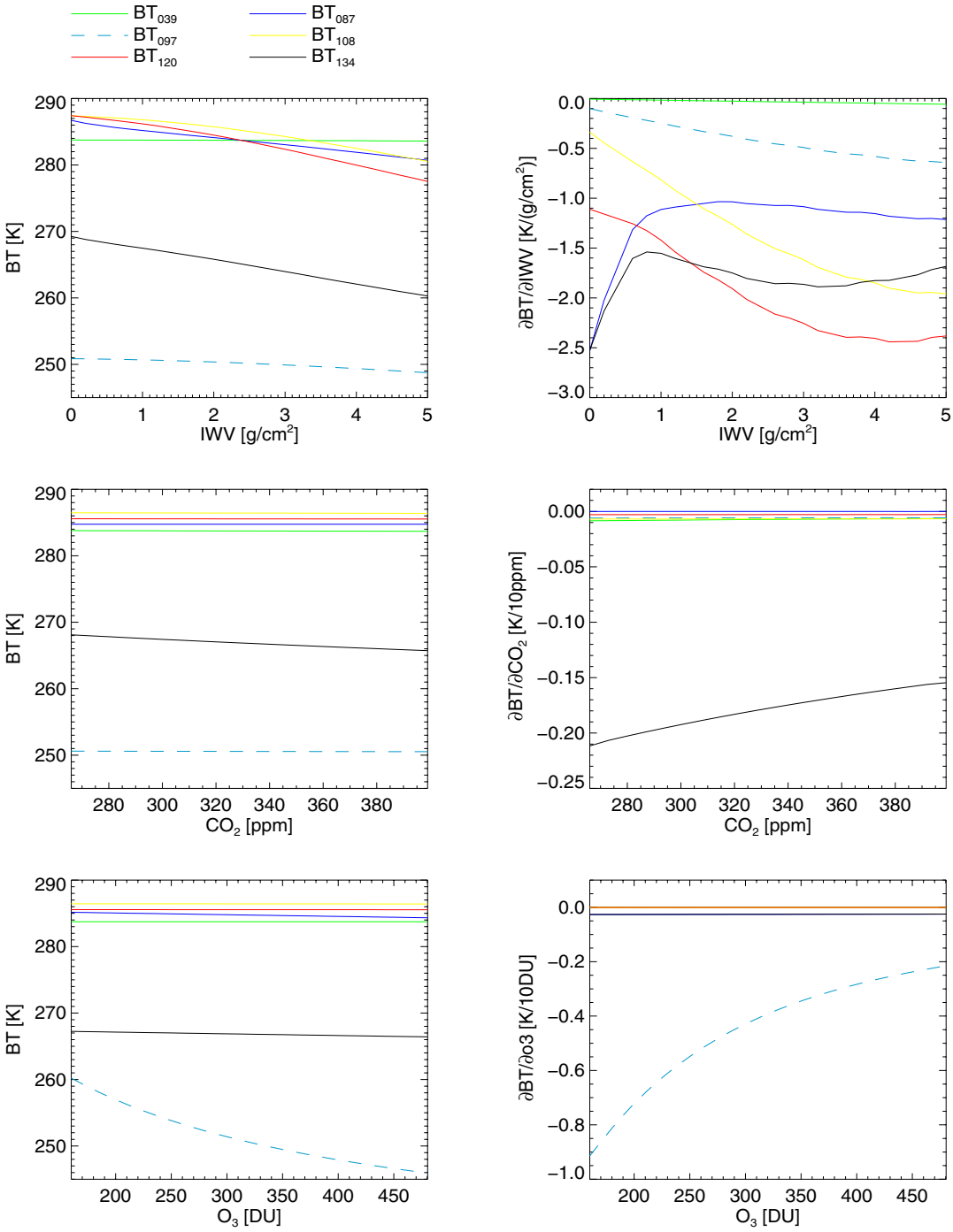

Figure 2-9: SEVIRI channel sensitivity to water vapor (**top**), carbon dioxide (**middle**), and ozone (**bottom**) derived by XTRA calculations for a US standard atmosphere. On the left hand side the simulated channel brightness temperatures are shown, while the right hand side illustrates their derivatives.

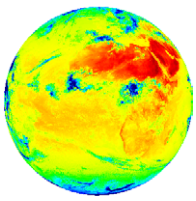

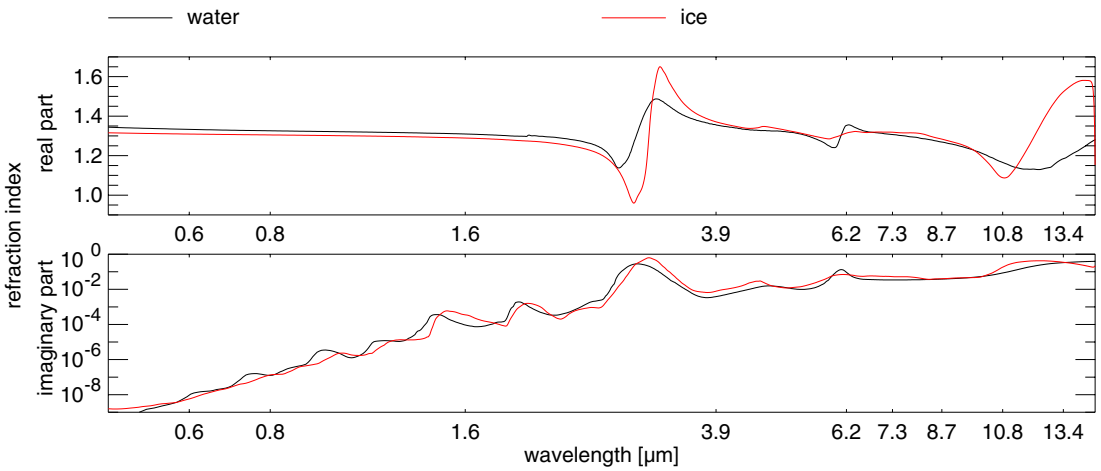

Figure 2-10: Real and imaginary part of the refraction index of water ($0.45\mu m \rightarrow 2\mu m$ from *Downing and Williams*, [1975], $2\mu m \rightarrow 15\mu m$ from *Segelstein*, [1981]) and ice [*Warren*, 1984].

the real part, primary affecting diffraction, are shown in figure 2-10. As will be discussed later, especially the channel NIR_{016} and IR_{039} provide information to discriminate water from ice clouds. The imaginary part of the refraction index of ice is almost four times higher at $1.6\mu m$ and two times higher at $3.9\mu m$. This causes higher absorption values for ice than for water at these wavelengths.

Resulting from Mie calculations, the asymmetry factor g_λ, the single scattering albedo $\omega_{s,\lambda}$, and the mass extinction coefficient σ_λ are shown in figure 2-11 for different droplet sizes. The mass extinction coefficient is defined as a sum of mass absorption coefficient $\sigma_{a,\lambda}$ and mass scattering coefficient $\sigma_{s,\lambda}$:

$$\sigma_\lambda = \sigma_{a,\lambda} + \sigma_{s,\lambda} \tag{2-13}$$

Just like the mass extinction coefficient, the single scattering albedo can take values from 0 to 1. It is defined as the ratio of scattering to total extinction:

$$\omega_{s,\lambda} = \frac{\sigma_{s,\lambda}}{\sigma_\lambda} \tag{2-14}$$

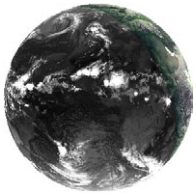

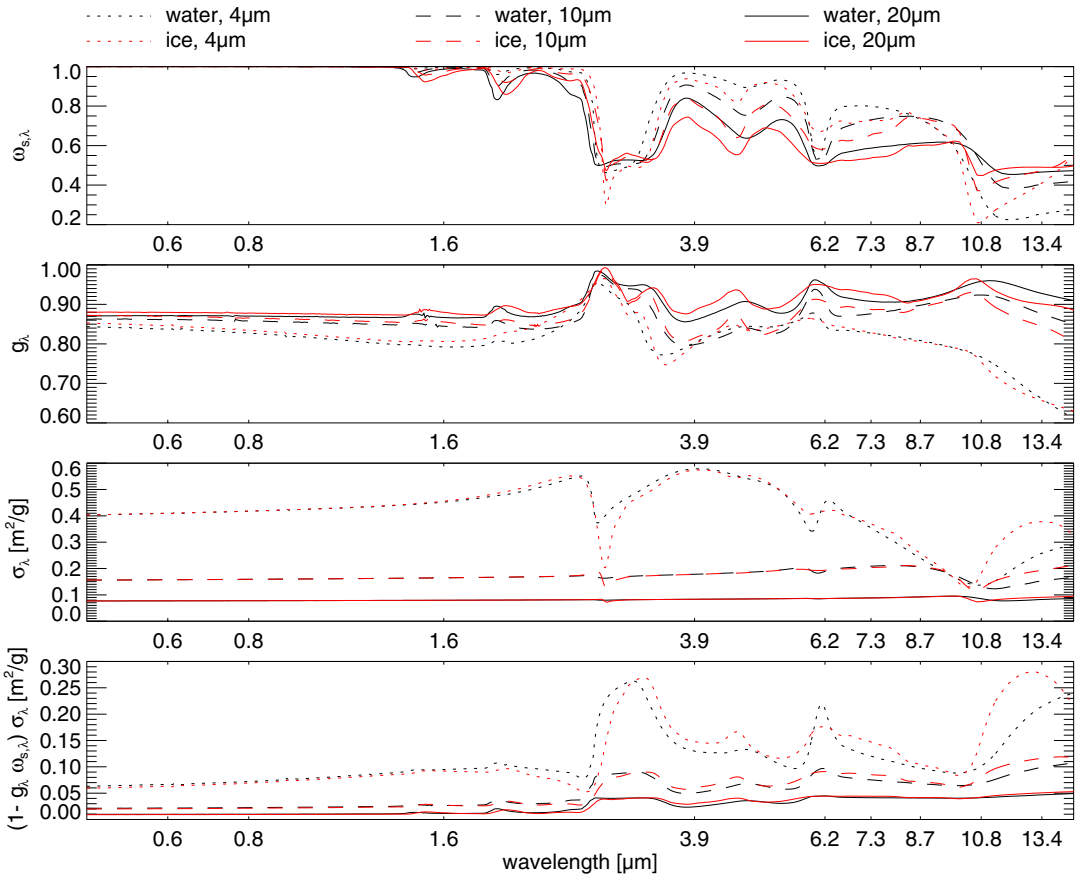

Figure 2-11: Resulting from Mie calculations for spherical ice as well as water particles with three different effective radii, this figure shows the single scattering albedo $\omega_{s,\lambda}$, the asymmetry factor g_λ, the mass extinction coefficient σ_λ, and the effective mass extinction coefficient $(1-g_\lambda\,\omega_{s,\lambda})\,\sigma_\lambda$. A modified gamma function has been chosen as particle size distribution.

The asymmetry factor represents the first moment of the scattering phase function (the mean cosine of the scattering angle). Possible values are in the range from -1 to 1.

Also included in figure 2-11 is the effective mass extinction coefficient σ_λ' which represents absorption and scattering in non-forward direction only:

$$\begin{aligned}\sigma_\lambda' &= (1-g_\lambda\,\omega_{s,\lambda})\,\sigma_\lambda \\ &= \sigma_\lambda - g_\lambda\,\sigma_{s,\lambda} \\ &= \sigma_{a,\lambda} + \sigma_{s,\lambda}\,(1-g_\lambda)\end{aligned} \qquad (2\text{-}15)$$

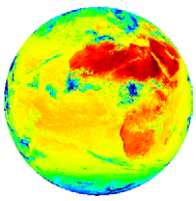

By means of the *delta-Eddington* approximation [*Joseph et al.*, 1976; *Deeter and Evans*, 1998] implemented in XTRA for parametrization of multiple scattering at cloud droplets, the emissivity, transmissivity, and reflectivity of a cloud layer can be calculated. Input parameters for this approximation are $\omega_{s,\lambda}$, σ_λ, g_λ, scaled variables analog to (2-15) and also the cloud's columnar total water path *TWP* (liquid and/or ice). Exemplary results for some water as well as ice clouds with a total water path of 500 $g\,m^{-2}$ are presented in figure 2-12. Increasing the total water path leads to similar results within the thermal infrared spectral region. The comparison of figure 2-11 with figure 2-12 shows, that the cloud emissivity and reflectivity is mainly affected by the single scattering albedo. On the basis of this example it can be suggested that in the visible and near infrared spectral region, channel NIR_{016} provides the most suitable information for retrieval of cloud droplet effective radius and cloud thermodynamic phase. The same applies for IR_{039} within the thermal infrared spectral region.

The penetration depth $p_{1/e}$ into a cloud, defined as the depth from which is still significantly contributed to the satellite's signal can be approximated as follows:

Assuming only single scattering, the cloud optical thickness τ_λ becomes:

$$\tau_\lambda = \sigma_\lambda' \, TWP \tag{2-16}$$

The reduction of radiation intensity passing a medium with given optical thickness is proportional to $e^{-\tau_\lambda}$. For the penetration depth defined by an intensity reduction of $1/e$ follows:

$$p_{1/e} = \frac{1}{\sigma_\lambda' \, \rho} \tag{2-17}$$

Results for a cloud with constant total water content per cubic meter $\rho = 0.5\ g\,m^{-3}$ are given in figure 2-13. It is obvious that the signal of the thermal infrared channels are only affected by comparatively thin layers at the cloud top. Especially for short wavelengths, the penetration depth is strongly dependent on the optical thickness and the droplet effective radius.

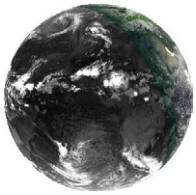

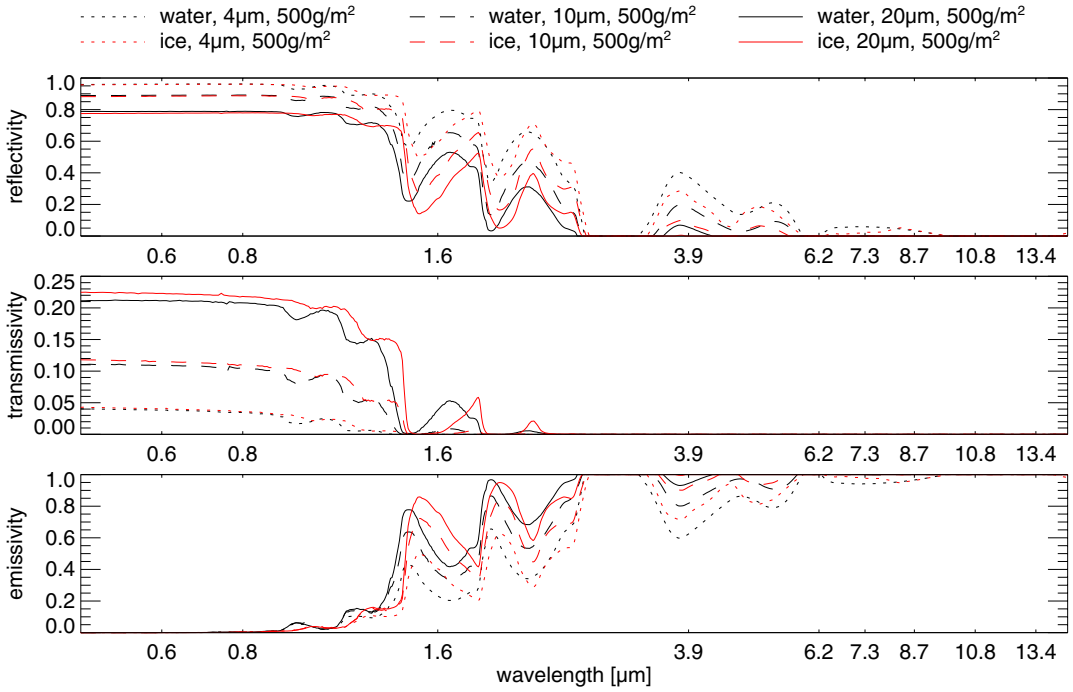

Figure 2-12: Emissivity, reflectivity, and transmissivity of water and ice clouds for three different effective particle radii and a columnar total water path of $500\,g/m^2$ resulting from the *delta-Eddington* approximation.

2. 5 Choosing suitable SEVIRI channels for cloud detection

The radiation measured by SEVIRI concerns radiation emitted by the earth's surface or atmosphere (including clouds and aerosols) and reflected solar radiation. Comparing the SEVIRI channel response functions (figure 2-2) to the flux of solar radiation at top of the atmosphere and to the radiation flux of a black body at $300K$ as approximation of the earth's emission (figure 2-14) points out the source of radiation measured in each channel: The comparison shows that the channels HRV, VIS_{006}, VIS_{008}, and NIR_{016} are not affected by thermal emission of the earth or the atmosphere. From figure 2-7 and figure 2-12 can be suggested that clouds as well as the majority of surface types in SEVIRI's field of view

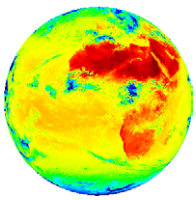

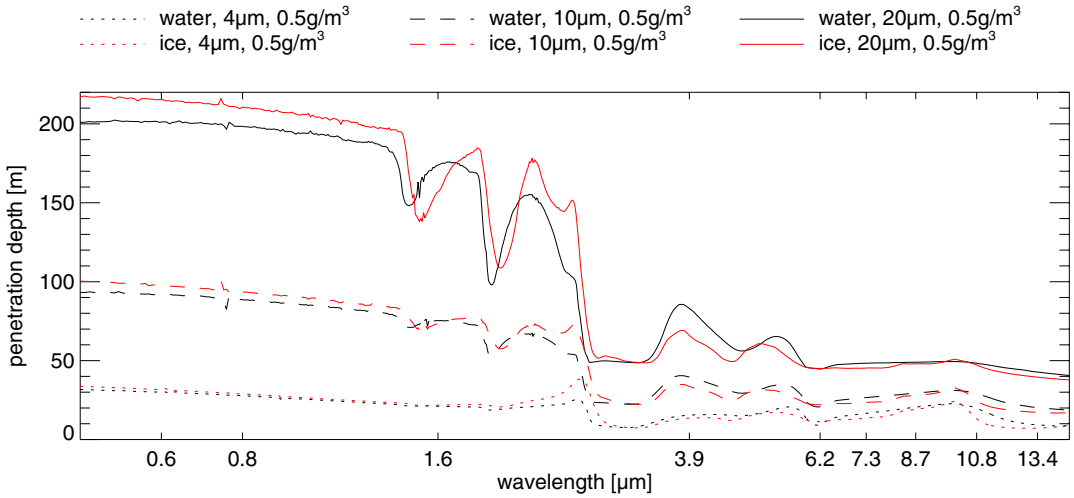

Figure 2-13: This figure shows the penetration depth of a cloud with constant total water content per volumen of $\rho = 0.5\ g\ m^{-3}$, defined as signal reduction by $1/e$ and assuming only single scattering (2-17).

have very low reflectivities in the range of 6 to 7.5μm. The incoming solar radiation at 7.5μm is already decreased to the 30th part of the 300K black body radiation. Due to these facts, neglecting the sun as source of radiation measured in the channels IR_{062}, IR_{073}, IR_{087}, IR_{097}, IR_{108}, IR_{120}, and IR_{134} is a valid approximation. The channel IR_{039} is different, it measures solar radiation as well as thermal radiation so that the behavior of this channel differs from daytime to nighttime which has to be considered in the algorithm design.

Figure 2-8 shows the effective transmissivity of a US standard atmosphere calculated by radiative transfer simulations of XTRA considering molecular absorption only. The effective transmissivities when taking the strong absorbing air mass constituents H_2O, CO_2, and O_3 separately into account are also illustrated in this figure. The strong influence of CO_2 absorption to $IR_{13.4}$, O_3 absorption to IR_{097}, and H_2O absorption to IR_{073} and IR_{062} becomes highly visible. The other channels are influenced only marginally by molecular absorption, like IR_{108} and IR_{120} which are affected by comparatively weak water vapor continuum absorption. The vertical density distribution in the atmosphere of these constituents mainly affects the normalized channel weighting function wf_{ch} of the

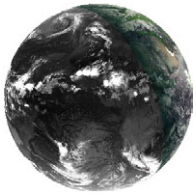

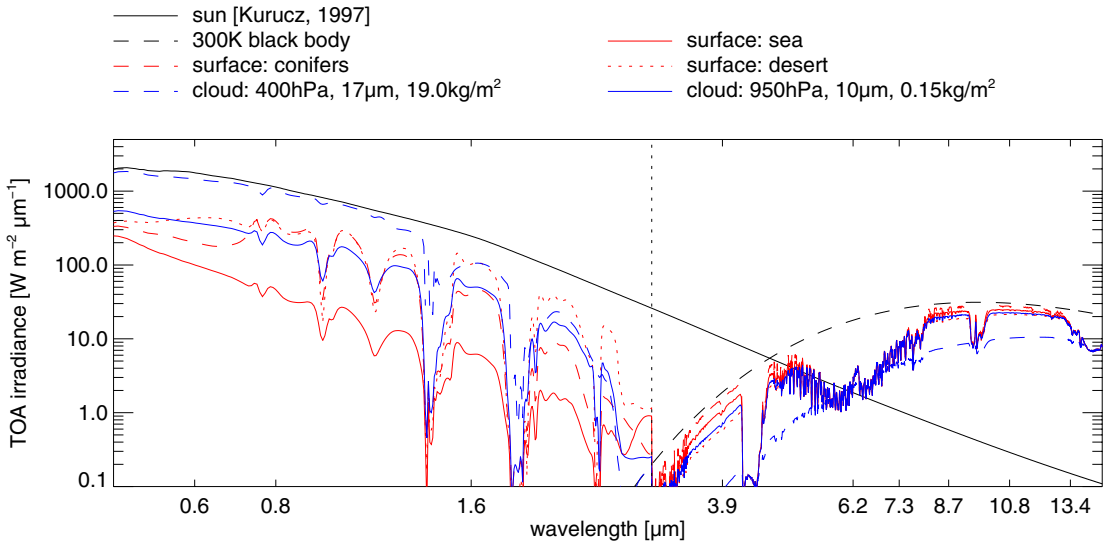

Figure 2-14: Illustrated are the top of atmosphere radiation fluxes of incoming solar radiation [*Kurucz*, 1997], the spectra of two simulated exemplary cloud covered atmospheres, and three simulated exemplary cloud free atmospheres, and also the radiation flux of a $300\,K$ black body. The simulated spectra have been derived using the radiative transfer programs MOMO, neglecting thermal emission, on the left hand side and XTRA on the right hand side, neglecting solar radiation. Thanks to Anja Hünerbein for providing the MOMO simulations.

thermal SEVIRI channels ch. In this context, weighting function is defined as signal sensitivity to temperature change ∂T of a $50\,hPa$ atmospheric layer depending on its pressure level p.

$$wf_{ch,p} = \frac{\partial L_{ch}}{\partial T_p} \tag{2-18}$$

This function has been calculated for each thermal SEVIRI channel by XTRA radiative transfer simulations for a US standard atmosphere. The results, given in figure 2-15, have been normalized to their maximum values. The weighting functions of IR_{062} and IR_{073} have their maximum values at around $400\,hPa$ and $600\,hPa$, respectively. The maximum of all other calculated weighting functions is at surface level meaning that these channels are primarily affected by the surface emission.

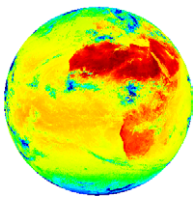

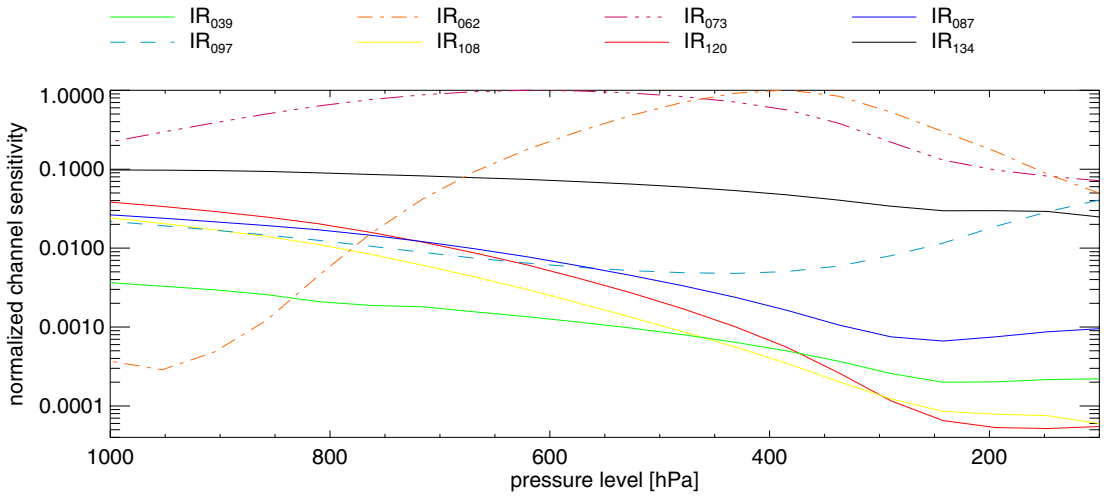

Figure 2-15: The SEVIRI thermal infrared channel's normalized weighting functions on a logaithmic scale, defined as signal sensitivity on temperature change of a $50\,hPa$ atmospheric layer at given pressure level according to (2-18). All channels except IR_{062}, IR_{073} show maximal sensitivity on temperature changes of the surface. The shown curves are results from XTRA simulations of a US standard atmosphere with a black body like surface.

For cloud detection, only the channels VIS_{006}, VIS_{008}, NIR_{016}, IR_{039}, IR_{087}, IR_{108}, IR_{120}, IR_{134} have been chosen as they have identical spatial resolutions and pixel co-locations and as they obtain enough information also from the lower atmosphere. Channel IR_{097} has been neglected due to its strong sensitivity to the total ozone concentration (figure 2-9) which is highly variable in the stratosphere and which is linked to processes not related to clouds. As shown in figure 2-9, the variability of BT_{097} can amount to up to $14\,K$ caused by different ozone concentrations in the range of 160 to $480\,DU$.

The data of all thermal infrared channels utilized by the cloud detection scheme is converted to brightness temperatures according to equation (2-8).

In the following, an overview of the channels chosen for cloud detection will be given. This will be done particularly with regard to the question how the presence or absence of clouds influences the signal in these channels.

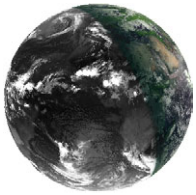

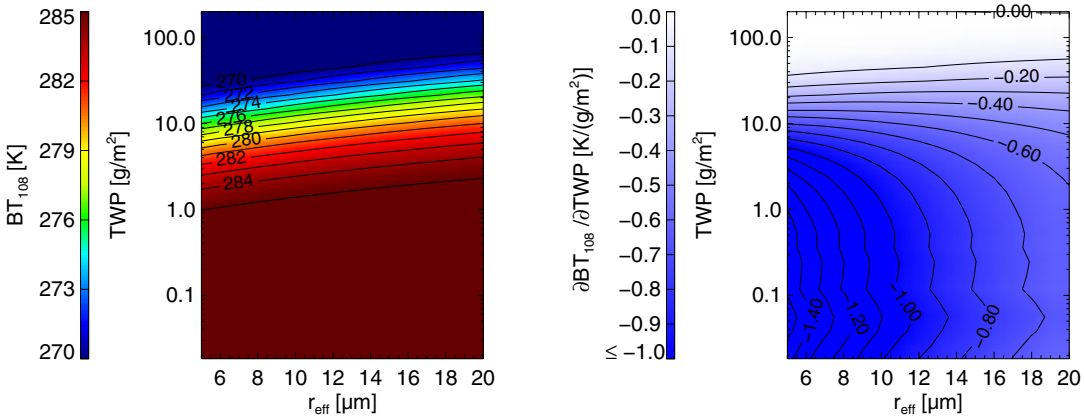

Figure 2-16: As result of XTRA simulations for a US standard atmosphere including one homogeneous water cloud layer at $700 hPa$, the left figure shows the simulated SEVIRI channel brightness temperature BT_{108} depending on the effective droplet radius r_{eff} and also on the total water path TWP, (logarithmic scale) while the figure on the right hand side illustrates the channel sensitivity to the total water path.

2. 5. 1 IR_{108} channel

Due to Mie scattering properties (figure 2-11), the penetration depth of clouds in this channel is comparatively low (figure 2-13). Hence, this channel's signal is considerably affected also by clouds with low total water path. Figure 2-16 illustrates the high signal sensitivity to the total water path, that amounts to up to $1.4\,K/(g/m^2)$ in the range of 0 to $50\,g/m^2$. Clouds with higher total water path than $80\,g/m^2$ almost saturate the signal, because at $10.8\mu m$ no significant part of the surface emitted radiation can pass through these clouds. According to figure 2-7 and figure 2-12, the possible target emissivities in this channel are all close to the emissivity of a black body. Furthermore, the continuum absorption of water vapor is relatively weak at $10.8\mu m$ (figure 2-8). For these reasons, the brightness temperatures measured in this channel are highly correlated to the target temperatures. Consequently, this channel is suitable for detecting clouds due to their temperature which is generally lower than the temperature of the surface beneath. For the same reasons, this channel was chosen for estimating diurnal cycles of the assumed clear

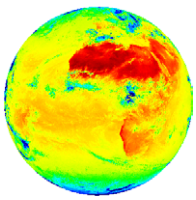

sky brightness temperature (chapter 3). Low brightness temperatures measured in this channel as well as high differences to the estimated clear sky brightness temperatures give an excellent indication for the presence of clouds. Nevertheless, the discrimination of fog or low stratus clouds and surface only from this channel is often not possible because of very low contrasts [*Ernst*, 1975]. As former METEOSAT satellites have only one channel in the thermal infrared window similar to the $10.8\,\mu m$ channel of SEVIRI, cloud detection techniques as developed by *Rossow and Garder* [1993a] for ISCCP are solely based on data of this channel during nighttime.

2. 5. 2 IR_{120} channel

The optical properties of surfaces and clouds in this channel are similar to those in IR_{108}, but they differ by stronger water vapor continuum absorption (figure 2-8) and stronger effective extinction by small ice particles (figure 2-11). Therefore, major positive brightness temperature differences $BT_{108} - BT_{120}$ indicate the presence of optical thin clouds with small droplets (figure 2-17) or a cloud free atmosphere with large water vapor content (figure 2-18), while minor differences indicate a dry atmosphere above surface or optical thick clouds. Therefore, the effect of differential extinction by small ice particles is often utilized for the detection of thin cirrus clouds [*Inoue*, 1987; *Giraud et al.*, 1997]. The effect of differential water vapor absorption is usable for the determination of the columnar water vapor content [e.g. *Harris and Mason*, 1992; *Chesters et al.*, 1987] and for atmospheric correction when deriving land and sea surface temperatures [e.g. *Sobrino et al.*, 1991; *Kerr et al.*, 1992]. Methods utilizing these brightness temperature differences are commonly called “split window” techniques.

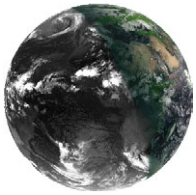

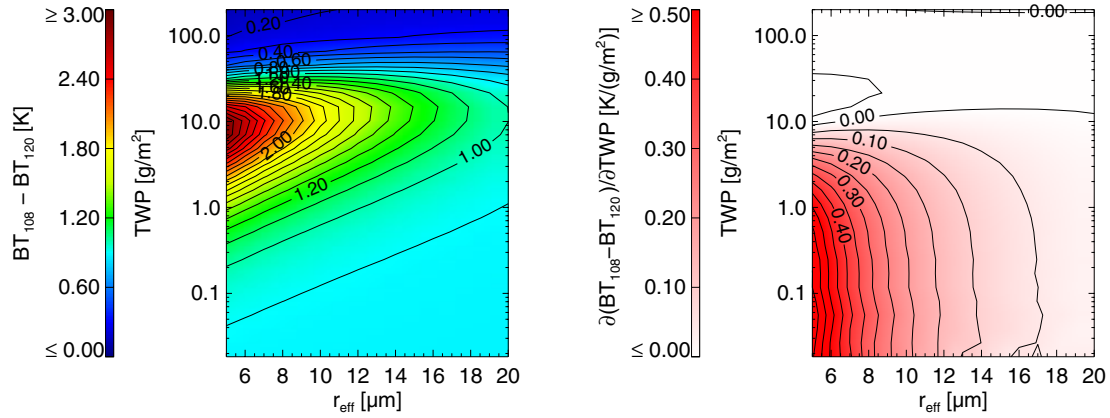

Figure 2-17: Resulting from the same XTRA simulations forming the basis of figure 2-16, this figure shows the channel difference $BT_{108} - BT_{120}$ as well as its sesitivity to *TWP*, both depending on the cloud total water path (logarithmic scale) and the cloud droplet effective radius.

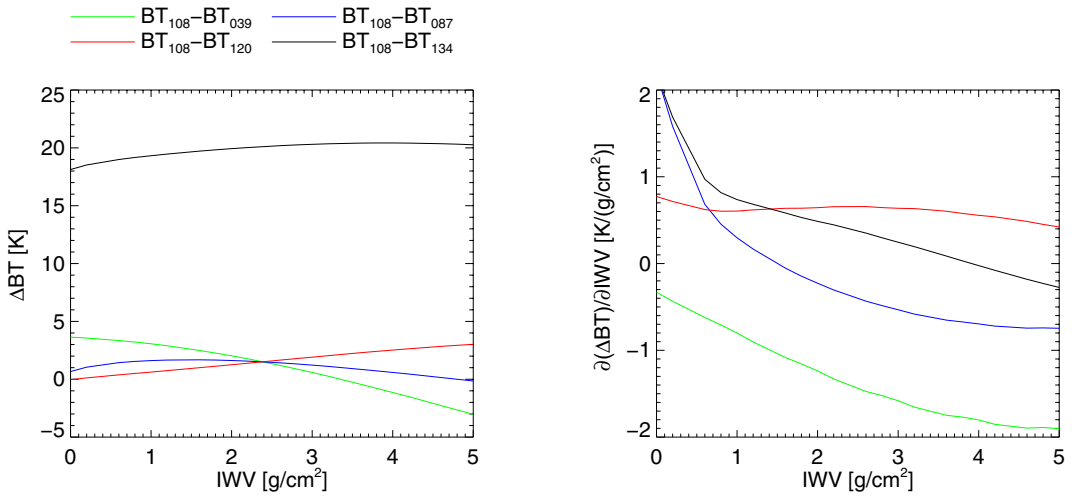

Figure 2-18: Sensitivity of several SEVIRI brightness temperature channel differences to the columnar integrated water vapor content *IWV* derived from XTRA simulations of a cloud free US standard atmosphere.

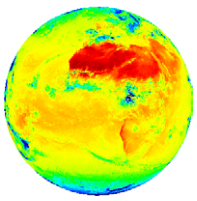

2. 5. 3 IR_{134} channel

As illustrated in figure 2-8 and figure 2-11 the water vapor continuum absorption as well as the extinction by Mie scattering at $13.4\mu m$ are similar to those at $12.0\mu m$. The main feature of this channel is its location at the CO_2 absorption edge (figure 2-8). Due to a nearly constant mixing ratio of CO_2 in the atmosphere, the weighting function of this channels shows significant signal sensitivity in all XTRA pressure levels (figure 2-15). For this reason the brightness temperature difference $BT_{134} - BT_{120}$ offers important information on the cloud top pressure. Figure 2-19 shows a nearly linear relation between $BT_{134} - BT_{120}$ and the cloud top pressure with a slope of around $-2.5K/100hPa$. This relation applies not only for clouds but also for most surfaces, because optical thick clouds and surfaces generally have similar emissivities in these channels (figure 2-7 and figure 2-12). This can be utilized to detect clouds due to their height above ground. A method to derive target heights from multiple channels at the CO_2 absorption edge is e. g. described in *Smith et al.* [1970] and *Menzel et al.* [1983].

2. 5. 4 IR_{087} channel

In consideration of cloud microphysical aspects, the behavior of IR_{087} is similar to IR_{108}, but for small droplets (effective radius less than $5\mu m$) the exemplary clouds shown in figure 2-12 exhibit weak emissivity reduction to a value of 0.96. Due to the relation between target emissivity and measured brightness temperature (figure 2-5, left), this results in positive brightness temperature differences $BT_{108} - BT_{087}$ of about $1.7K$ for clouds with small droplets and high total water paths (figure 2-20, left). As mentioned in the "MSG interpretation guide" [*EUMETSAT*, 2004e] this effect is applicable for discriminating fog from surface. In consequence of marginally less absorption by water vapor (figure 2-8), the difference $BT_{108} - BT_{087}$ shows also weak sensitivity to water

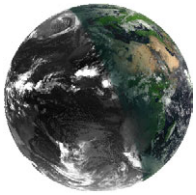

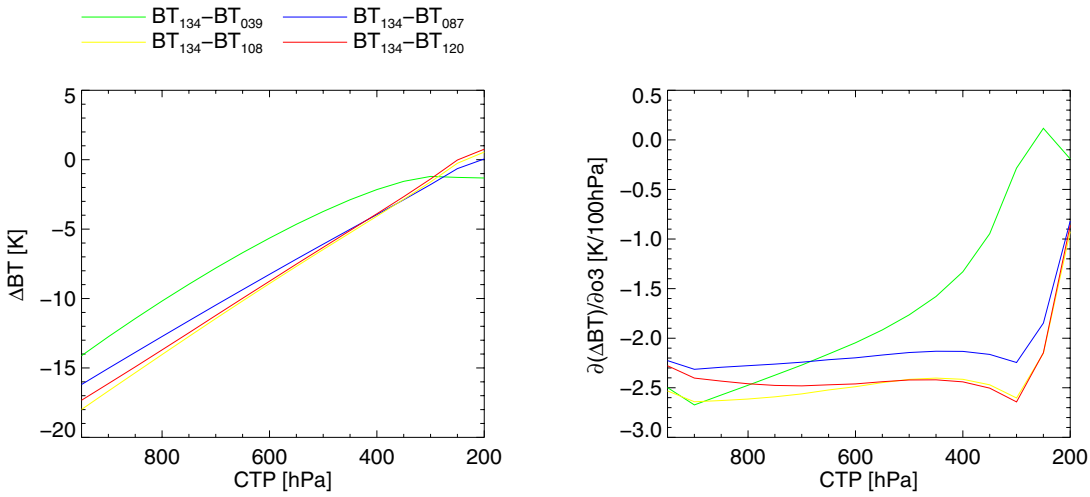

Figure 2-19: Sensitivity of several channel differences to the cloud top pressure *CTP*. Shown are results of XTRA simulations for a US standard atmosphere, including one water cloud layer with total water path of $200\,g/m^2$ and droplet effective radius of $16\mu m$. The figure on the right shows that there is considerable sensitivity of e.g. $BT_{134} - BT_{120}$ to the cloud top pressure even for low clouds.

vapor concentration (figure 2-18). However the most remarkable feature of this channel is the very low emissivity of xeric, sabulous surfaces. As shown in figure 2-5 and in *Gao and Wiscombe* [1994], this can also result in large positive $BT_{108} - BT_{087}$ differences of around $5K$ when assuming channel emissivities of $\varepsilon_{108} = 1.0$ and $\varepsilon_{087} = 0.9$. This can be used for discriminating clouds from deserts with similar temperatures (e.g. at nighttime).

All three phenomena described above lead to positive differences $BT_{108} - BT_{087}$ which often makes the interpretation ambiguous.

In *Ackerman et al.* [1990] and *Strabala et al.* [1994] a trispectral method for detecting clouds and deriving cloud phase from observations at $8\mu m$, $11\mu m$, and $12\mu m$ is proposed. This method is also applicable to the corresponding SEVIRI channels.

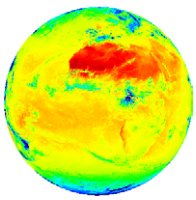

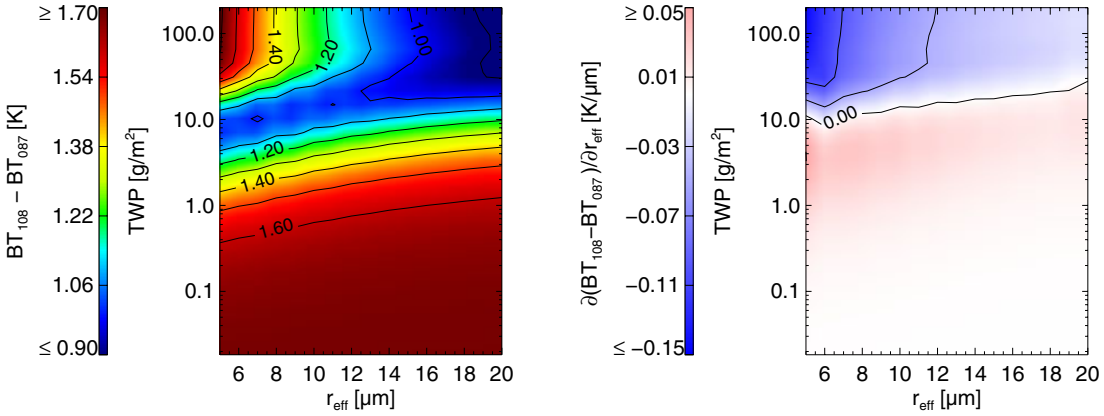

Figure 2-20: Resulting from the same XTRA simulations forming the basis of figure 2-16, this figure shows the channel difference $BT_{108} - BT_{087}$ as well as its sesitivity to r_{eff}, both against the cloud total water path (logarithmic scale) and the cloud droplet effective radius. Distinguishable there is a weak sensitivity to r_{eff} even for clouds that are optically thick.

2. 5. 5 IR_{039} channel

As discussed in the introduction of section 2. 5, IR_{039} is the only SEVIRI channel, whose signal is affected by thermal radiation of the earth and atmosphere as well as by reflected solar radiation. Therefore, the interpretation is different at nighttime and daytime which has to be considered in algorithm design.

IR_{039} is least affected by water vapor continuum absorption (figure 2-8), but there is a weak impact of carbon dioxid absorption (figure 2-8) that has to be considered for transversal viewing geometries.

Distinguishing low clouds from surfaces with the same temperature is very difficult when using only thermal information around $10.8\mu m$ [*Ernst*, 1975]. For this task, IR_{039} provides important additional information at daytime as well as at nighttime. The examples in figure 2-12 show that clouds, particularly those with small droplets, provide significantly lower emissivities than most non-xeric surfaces (figure 2-7). For nighttime, the sensitivity study shown in figure 2-21 illustrates that the brightness temperature

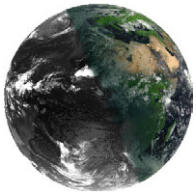

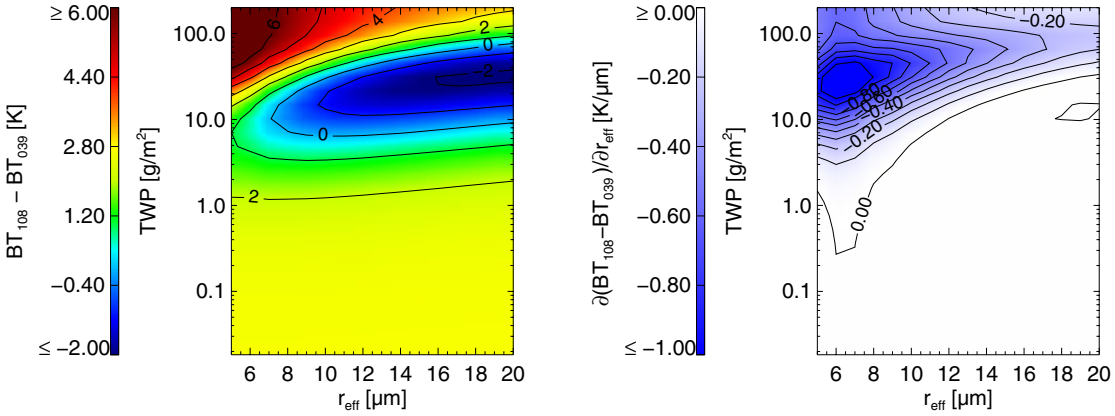

Figure 2-21: Analog to figure 2-20 these figures are resulting from the same XTRA simulations forming the basis of figure 2-16. Illustrated is the channel difference $BT_{108} - BT_{039}$ as well as its sesitivity to r_{eff}, both depending on the cloud total water path (logarithmic scale) and the cloud droplet effective radius. Highly visible is a considerable sensitivity to r_{eff} even for optically thick clouds.

difference $BT_{108} - BT_{039}$ can be increased by the presence of clouds with small droplets from less than $2K$ to more than $6K$. The interpretation has to be done carefully. Some xeric surfaces provide emissivities of less than 0.8. As given by figure 2-5, an emissivity reduction from 1.0 to 0.8 can result in a brightness temperature BT_{039} reduction of around $4K$. Assuming an emissivity close to one at $10.8\mu m$ results in just as high temperature differences $BT_{108} - BT_{039}$.

At daytime, the radiance L_{039} also includes a solar part and the conversion to brightness temperature BT_{039} according to (2-8) results only formally in a temperature value.

Especially water clouds with small droplets have a lower emissivity but a higher reflectivity at $3.9\mu m$ than most non-xeric surfaces (figure 2-7, figure 2-12). The effect of their higher reflectivity dominates, so that they cause more outgoing radiation in L_{039} than surfaces of the same temperature. At twilight conditions both effects can extinguish each other.

Therefore, this channel can be used to discriminate clouds from snow at daytime and also at nighttime. Some fog and low stratus detection methods utilizing data of spectral channels around $3.9\mu m$ are described in *Eyre et al.* [1984], *Lee et al.* [1997],

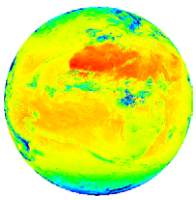

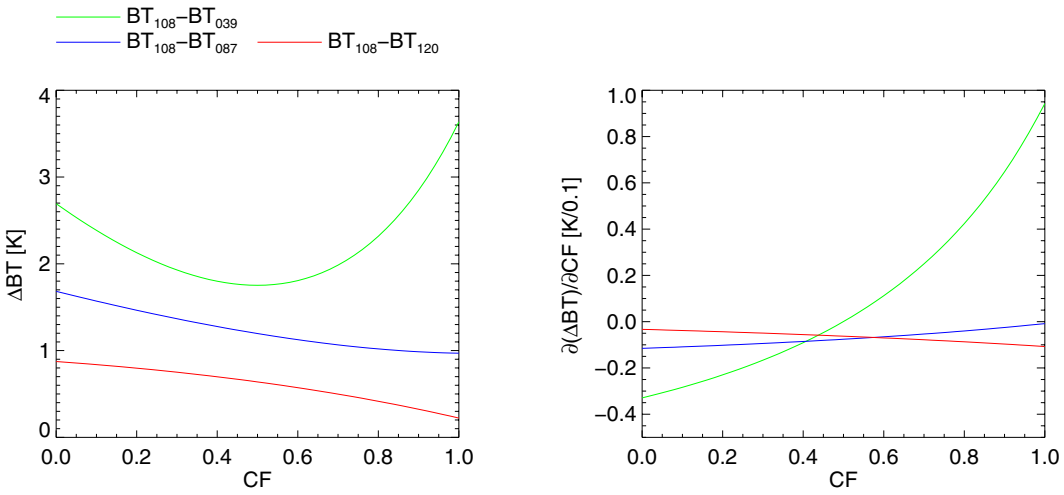

Figure 2-22: In figure 2-6 was shown, that the non-linearity of Planck's function leads to different channel brightness temperature sensitivities to the sub pixel temperature fraction. By means of XTRA simulations for a US standard atmosphere including one cloud layer at $700\,hPa$ with an total water path of $200\,g/m^2$ and cloud droplet effective radius of $16\,\mu m$, this figure exemplarily quantifies the effect of different channel sensitivities to the sub pixel temperature fraction.

Kudoh and Noguchi [1991], and *Anthis and Cracknell* [1999]. A method for discriminating snow/ice from clouds at daytime using the $3.75\,\mu m$ channel of AVHRR is described in *Xiong et al.* [2004].

For a simplified example of a signal mixed from two black bodys at $250\,K$ and $300\,K$, figure 2-6 shows that there is a non-linear relation between the channel brightness temperature and the pixel internal temperature composition. The non-linearity is most pronounced for the IR_{039} channel that is most sensitive to hot spots in the field of view. Hence, IR_{039} is also useful for fire detection [e.g. *Ichoku et al.*, 2003]. The sensitivity study illustrated in figure 2-22 shows that the variability of $BT_{108} - BT_{039}$ due to the pixel internal cloud fraction amounts approximately to $2\,K$ for this exemplary cloud. Accordingly, differences in brightness temperature of less than $2\,K$ may also be a result of broken clouds.

2. 5. 6 VIS_{006} channel

Except for snowy, sun glint-affected, or xeric surfaces, the majority of surface targets present relatively low reflectance values in the $0.6\mu m$ channel (figure 2-7) which causes high contrasts to clouds that often provide albedos of 0.8 and more in this channel (figure 2-12). Accordingly, this channel is most suitable to detect clouds because of their high reflectance. In particular the detection of low stratus clouds showing minor contrasts in the thermal infrared channels, can significantly be improved under utilization of the VIS_{006} channel. Channels in this spectral region are commonly used for cloud detection [e.g. *Rossow and Garder*, 1993a; *Ackerman et al.*, 1998] and retrieval of cloud optical thickness [e.g. *Evans and Haigh* 1995].

2. 5. 7 VIS_{008} channel

The contrast of clouds above vegetation covered surfaces in this channel is lower than in the VIS_{006} channel because of "red edge" reflection of green vegetation (figure 2-7). The molecule and aerosol scattering at $0.8\mu m$ is lower than at $0.6\mu m$. Due to this reason and an almost black ocean at $0.8\mu m$, the cloud/surface contrast over sea surfaces is higher in the VIS_{008} channel than in the VIS_{006} channel. As mentioned in *Watts et al.* [1998], in some publications [e.g. *King et al.*, 1992, 1997] the channel at $0.8\mu m$ is preferred for cloud optical thickness retrieval for the same reasons. Due to the fact that clouds are not only bright but also white in the visible spectral region (figure 2-12), this channel provides important additional information to discriminate clouds from bright surfaces except for snow or water with sun glint that are all also bright and white.

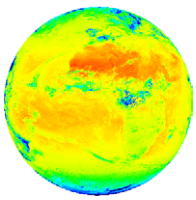

2. 5. 8 NIR_{016} channel

Compared to the reflectivity of snow (exemplarily given in figure 2-7), the reflectivity of clouds (exemplarily given in figure 2-12) is substantially higher at 1.6μm. Due to significantly more radiation absorption of ice compared to water at 1.6μm, illustrated by the imaginary part of the refraction index (figure 2-10), water clouds, with their higher reflectivity (figure 2-12), stand out from snow much better than ice clouds in this channel. Therefore, the NIR_{016} channel is extremely valuable to discriminate low water clouds from snowy surfaces at daytime. The usage of the corresponding MODIS channel for the MODIS cloud detection is described in *Ackerman et al.* [1998] and more detailed in *Ackerman et al.* [2002].

In addition to cloud detection, this channel is also useful for deriving cloud optical thickness and cloud droplet effective radius with the method introduced in *Nakajima and King* [1990]. Referring to *King et al.* [1997], it can be enhanced for also deriving the cloud thermodynamic phase.

2. 6 Temporal features of the 10.8μm channel brightness temperature

On the basis of some examples, this subchapter is supposed to illustrate typical time series of measured brightness temperatures BT_{108}. The characteristics of diurnal cycles and of brightness temperature measurements at consecutive days at a certain time of day will be analyzed.

In the latter subchapter it was shown, that BT_{108} is more correlated to the target temperature than any another SEVIRI channel. In this channel most of the possible targets in the field of view of SEVIRI exhibit an emissivity close to one (figure 2-7, figure 2-12), the absorption due to atmospheric water vapor in this spectral region is relatively weak (figure 2-8, figure 2-18), and the absorption of other gases is even negligible (figure 2-8).

In addition, it was shown that BT_{108} is highly sensitive to the appearance of clouds. Clouds with a total water path of approximately 80 g/m^2 are already saturating the signal and can decrease the clear sky brightness temperature by several $10K$ (figure 2-16).
Referring to the assumed clear sky brightness temperature estimation method introduced in chapter 3, the estimation of non-cloud-induced maximal brightness temperature changes in time series from SEVIRI pixels is of special interest and will be discussed in the following.

2. 6. 1 Intra-diurnal time series

Some exemplary BT_{108} diurnal cycles ("intra-diurnal time series") from June, 2nd 2004 are illustrated in figure 2-23. The selection of the pixel locations was made under the aspect to choose preferably non-cloud-contaminated diurnal cycles of different atmospheric conditions in SEVIRI's field of view. Importance was given to xeric regions due to their well-known high intra-diurnal surface temperature variability.
As shown in *Göttsche and Olesen* [2001], the following equation is suitable for fitting surface temperature diurnal cycles with adjustment of the parameters residual temperature around sunrise T_0, temperature amplitude T_a, width of cosine term ω, and the temperature difference $\delta T = T_0 - T|_{t \to \infty}$ related to the change of T_0 between two days:

$$T = \begin{cases} T_0 + T_a \cos\left[\frac{\pi}{\omega}(t - t_m)\right] & ;t < t_s \\ T_0 + \delta T + \left(T_a \cos\left[\frac{\pi}{\omega}(t_s - t_m)\right] - \delta T\right) e^{-(t-t_s)/k} & ;t \geq t_s \end{cases} \quad (2\text{-}19)$$

The parameters time of maximum t_m and start of the attenuation function t_s are given by the solar time. The attenuation constant k can be calculated by assuming differentiability at t_s.

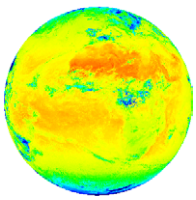

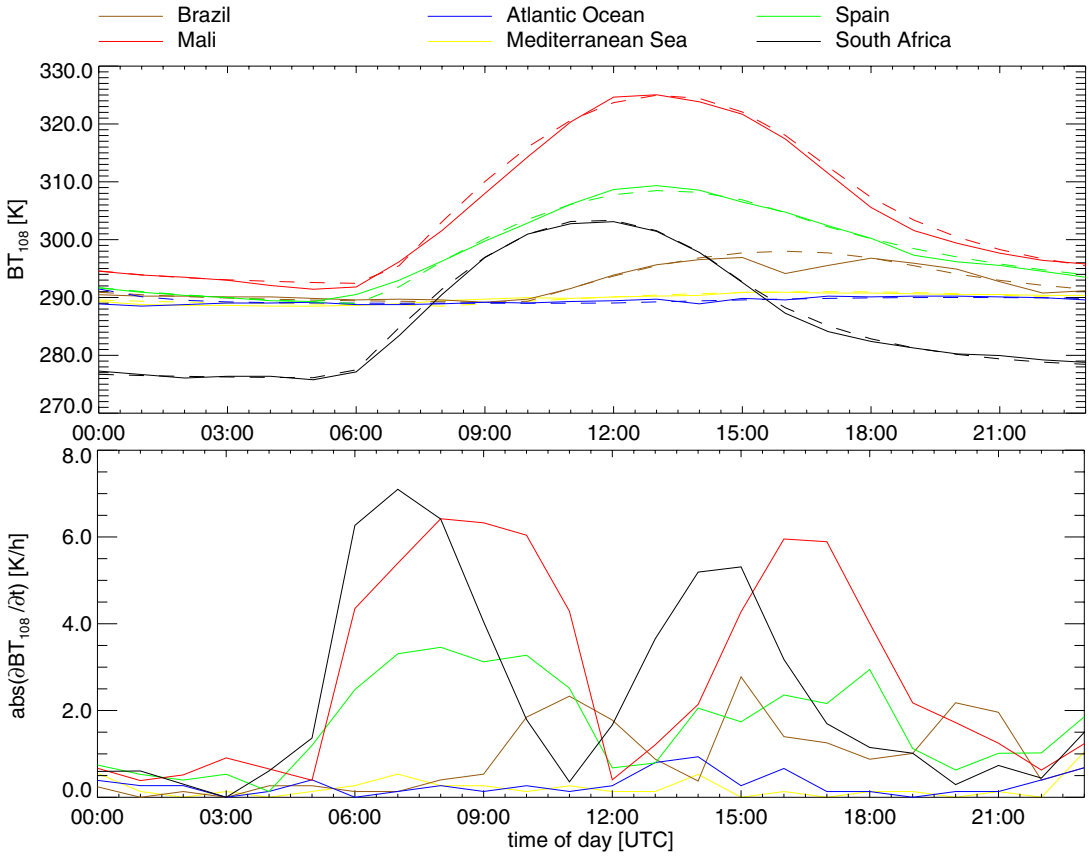

Figure 2-23: This figure shows some exemplary diurnal cycles of BT_{108} from June, 2nd 2004 (**top**). The illustrated diurnal cycles have been chosen to be preferably cloud free and to represent common surface types in SEVIRI's field of view. Also shown are their temporal derivatives (**bottom**) and curve fittings (**dashed**) according to equation (2-19).

For all diurnal cycles illustrated in figure 2-23, curve fittings could been found by means of the latter equation. These fittings are represented by dashed lines in figure 2-23. The manually adjusted parameters as well as the calculated attenuation constants were all in physical reasonable range similar to those given in the publication referenced above.

In addition, figure 2-23 also contains the absolute values of the temporal derivatives of the measured brightness temperature diurnal cycles. Expectedly, the xeric regions provide the highest temperature changes with up to $7\,K/h$, whereas the brightness temperature

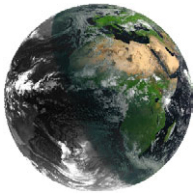

changes of the Atlantic Ocean measures less than $1\,K/h$. The weak discontinuity at 16:00 UTC in the diurnal cycle of the pixel located in Brazil is probably caused by sub pixel cloudiness.

2. 6. 2 Extra-diurnal time series

In this context "extra-diurnal time series" stands for time series accumulated from measurements of consecutive dates at specific pixel location and specific times of the day. Considering the same aspects as in the latter section some exemplary preferably cloud free extra-diurnal time series from June, 1st 2004 until July, 31st 2004 always at 12:00 UTC have been acquired. These time series as well as the corresponding temporal derivatives are illustrated in figure 2-24. Additionally, this figure shows the results of a manual cloud classification coded with different plot symbols.

The time series from water surfaces are holding the lowest temperature variabilities between two consecutive days, measuring less than $2\,K/day$ except for two cases with around $3.3\,K/day$ and a mean value of $1\,K/day$. As expected, the time series of brightness temperature derivatives of land surfaces shown in this figure are greater. These are limited by around $7.8\,K/day$, measured for the pixels in Spain and Algeria. The mean temperature gradient of the investigated land surfaces amounts to $2\,K/day$.

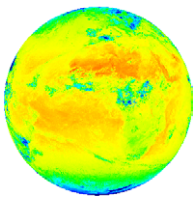

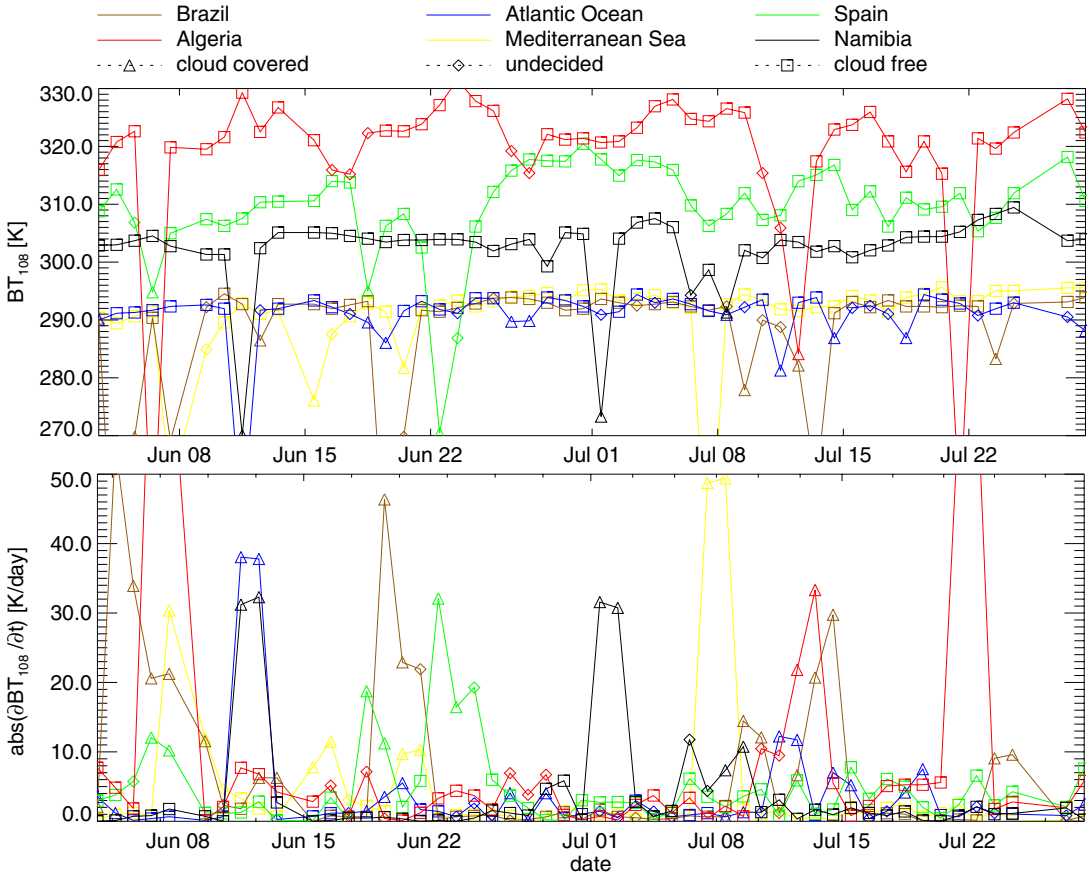

Figure 2-24: On the same conditions as the diurnal cycles shown in figure 2-23, extra-diurnal time series of BT_{108} have been selected consisting of consecutive brightness temperature measurements at 12:00 UTC from June, 1st 2004 to July, 31st 2004. These time series (**top**) as well as their temporal derivatives (**bottom**) are shown in this figure. Additionally, the results of a manual cloud identification (utilizing several SEVIRI channels) are included in this figure by using different plot symbols (see plot legend). The symbols within the curves of the temporal derivative have been applied considering at each time two consecutive values. In this way the cloud free symbol is only applied if there are two consecutive cloud free classifications.